Impacts of Local Convective Processes on Rain on the Caribbean Island of Puerto Rico

N. Hosannah[1] [ID], **J. E. González[2], C. Lunger[2], and D. Niyogi[3]** [ID]

[1]Department of Mathematics, Engineering, and Computer Science, LaGuardia Community College, Long Island City, NY, USA, [2]NOAA CREST and Department of Mechanical Engineering, The City College of New York, New York, NY, USA, [3]Department of Agronomy - Crop, Soil and Environmental Sciences, and Department of Earth, Atmospheric and Planetary Sciences, Purdue University, West Lafayette, IN, USA

Abstract This study aims to determine the impacts of tropical island processes on local convective storms. An analysis of rain events on the island of Puerto Rico between 1 June 2015 and 31 July 2016 showed that local island-enhanced western storms accounted for 89 of 322 storms. This period is of particular importance for the Caribbean as 2015 was one of the driest years on record. While large-scale influences such as the El Niño–Southern Oscillation, the North Atlantic Oscillation, African easterly waves, and Saharan dust transport modulate moisture conditions in the region, correlations between precipitation and El Niño–Southern Oscillation (−0.14), North Atlantic Oscillation (−0.42), and Saharan dust (0.1) for 1980–2016 ranged from weak to moderate. Local data for the island of Puerto Rico from weather stations, the Convection, Aerosol, and Synoptic-Effects in the Tropics field campaign, and the North American Mesoscale model support the initiation or enhancement of convective rain events due to local island processes. In particular, analysis of surface wind speed/direction, convective available potential energy, lifted index, and the bulk Richardson number substantiate local instability due to surface heating, orographic uplift, and sea breeze trade-wind convergence. These convective forcings along with available precipitable water in excess of 50 mm ultimately led to intense storms despite severe rainfall-mitigating dust episodes for which aerosol optical thickness exceeded 0.4. These results may have major implications for considering the impacts of local air-sea-land interactions on rainfall over other tropical islands.

1. Introduction

Some of the highest annual precipitation totals in the world occur in tropical coastal environments near high elevations and are subjected to strong sea breeze such as Lloro (Colombia), Debundscha (Cameroon), and Kauai (Hawaii), which report annual totals exceeding 10,000 mm (Krause & Flood, 1997). While large-scale surface-atmospheric conditions are the first-line drivers of precipitation in these environments, local-scale dynamics are also critical to convection and precipitation (Jury, 2009; Liu & Moncrieff, 1996). Multiscale influences are extremely important in the Caribbean basin (85–60°W, 8–22°N), a relatively land-free tropical area home to over 43 million inhabitants (Population Reference Bureau, 2016), and understanding the region's multiscale hydro-climatic drivers is necessary for the well-being of the Caribbean Islands (Food and Agriculture Organization of the United Nations, 2016; United Nation Environment Programme, 2008).

Annual rainfall totals over the island of Puerto Rico range from 768 mm in the south to 4,305 mm in the east (Gómez-Gómez et al., 2014), and like many other Caribbean islands, its moisture is modulated by large-scale contributors such as the El Niño–Southern Oscillation (ENSO), the North Atlantic Oscillation (NAO), and Saharan dust. These variables combined with the island-scale mechanical redirecting of easterly winds by mountain ranges and thermally induced land-sea interaction near coasts lead to varied precipitation climatologies across the island. These variations can be observed even during intense dry spells. During the extreme drought in 2015, rainfall deficits exceeded 200 mm as early as April 2015, and the hardest hit municipalities were in eastern Puerto Rico (Coto, 2015a, 2015b; Feiser, 2015). The west side was less affected, with some sites exhibiting positive precipitation anomalies. Puerto Rico is an ideal Caribbean Island to study these locality variations because of its good hydrometeorological data record and sensor network. As a result we herein investigate local convective storms in western Puerto Rico, with the greater purpose of understanding how land-sea-air interactions may

enhance storm production in a coastal tropical environment. In the subsequent two sections, we discuss regional- (section 1.1) and island-scale (section 1.2) impacts on rainfall.

1.1. Large-Scale Impacts on Caribbean Rain

The ENSO, NAO, and Saharan dust impact Caribbean surface-atmospheric conditions, which may contribute to the region's bimodal annual precipitation climatology, characterized by a lull in rainfall totals during June–July, after which totals increase (Angeles et al., 2010). This rainfall reduction occurs in the eastern Caribbean in late June and toward the western Caribbean during July (Gamble et al., 2008; Gamble & Curtis, 2008).

1.1.1. ENSO and NAO

The ENSO modulates both sea surface temperatures (SSTs) and the atmospheric circulation- modifying evaporation rates and cloud formation over tropical waters (Taylor et al., 2002). The El Niño phase is associated with reduced sea level pressure (SLP) and enhanced deep convection in the anomalously warmer tropical Pacific, correlating with higher SLP and intensified vertical wind shear in the cooler tropical Atlantic and Caribbean (Giannini, Chiang, et al., 2001; Taylor et al., 2002; Wang, 2005; National Oceanic and Atmospheric Administration, 2014; Knaff et al., 2004). The strong regional convection in the Pacific and the altered jet stream promotes a drier July–October period in the Caribbean (Birgmark, 2014; Gray, 1967, 1968; Kingtse et al., 2001).

The NAO is a north-south dipole of SLP anomalies with the low pressure centered in Greenland and the North Atlantic High Pressure (NAHP) centered between 35°N and 45°N. NAO impacts synoptic moisture transport (Hurrell, 1995), leading to temperature and precipitation modification (Rogers & van Loon, 1979; van Loon & Rogers, 1978; Walker & Bliss, 1932). A positive (negative) NAO phase relates to a stronger (weaker) NAHP, which generates surface easterly wind anomalies (Giannini, Chiang, et al., 2001). The wind-evaporation-SST feedback (Qu et al., 2012) links the Caribbean and the NAHP, as when SLP increases (decreases) the easterly winds intensify (weaken) causing more (less) evaporation, cooler (warmer) SSTs, and reduced (increased) convection. As the NAHP intensifies during July (Hastenrath, 1976, 1978; Malmgren et al., 1998), increased cloud cover extends negative SST anomalies (Angeles et al., 2010; Giannini et al., 2000, Giannini, Cane, & et al, 2001). Thus, drier summers partly associated with El Niño onset are exacerbated when a positive winter NAO phase is observed prior (Giannini, Cane, et al., 2001).

1.1.2. Saharan Dust and African Easterly Waves

The hot, dry Saharan desert contrasts the cooler, wetter Gulf of Guinea resulting in the African easterly jet, a flow of nonconstant, high-speed, high-altitude winds (Burpee, 1972; Rennick, 1976). The resulting north-south undulations form westward traveling easterly waves that become a vital conduit for Caribbean moisture (Grist, 2002; Landsea et al., 1998; Thorncroft & Hodges, 2001). With adequate moisture, lift, and instability, easterly waves produce bands of thunderstorms, and sometimes merge with air circulations to form tropical cyclones. Easterly waves reach their peak (nadir) frequency during the summer (winter) and last from days to several weeks traveling at 5–7 m/s. In addition, Saharan dust travels toward the Caribbean in a Saharan Air Layer (SAL) that may extend to 6 km agl (Carlson & Prospero, 1972; Reid et al., 2002;Prospero & Lamb, 2003). Saharan dust may quell easterly waves and inhibit convection via convective capping (Dunion, 2011) and rainfall via suppressed cloud droplet growth due to increased aerosol concentrations (Angeles et al., 2010; Dunion & Velden, 2004; Hosannah et al., 2015; Ismail et al., 2010; Jaenicke & Schütz, 1978; Rosenfeld et al., 2001).

1.1.3. Summer Rainfall Over the Caribbean Islands

Monthly precipitation normals from the Caribbean Institute of Meteorology and Hydrology and the National Climate Data Center show a rainfall reduction during June and July coincident with particle concentration (derived from Aerosol Robotic Network, AERONET) increases at multiple Caribbean locations (Figures 1a and 1b), suggesting that a feedback relationship exists between dust intensity and rainfall. Barbados (13.17 N, 59.50 W), the most eastern site, is the only locality that does not register a precipitation dropoff in June–July. Western sites, such as Camaguey, Cuba (21.14°N, 77.85°W) and Key Biscayne, Florida (25.73°N, 80.16°W) exhibit a later dropoff.

The varied conditions at three sites in Puerto Rico (San Juan [18.38°N, 65.62°W], La Parguera [17.97°N, 67.05°W], and Mayaguez [18.21°N, 67.14°W]) are also exhibited, where Mayaguez in the west is the wettest, and La Parguera in the southwestern dry forest is the driest. Mote et al. (2017) examined the SAL effects on
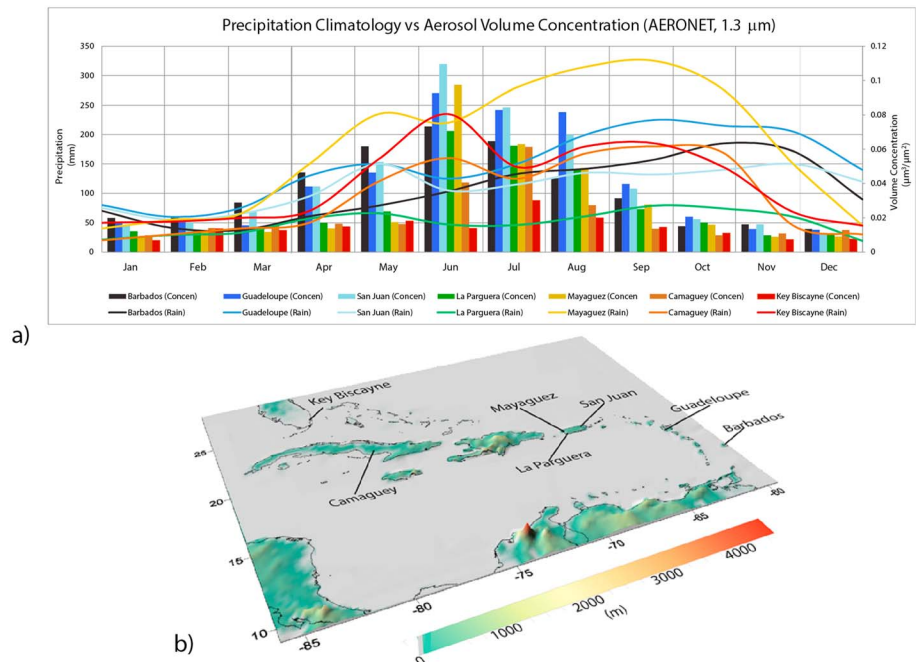
Figure 1. (a) Average monthly precipitation (lines) and AERONET aerosol volume concentration (bars, denoted by *concen*) at multiple sites. (b) Regional topographical map.

the 2015 drought in eastern Puerto Rico, and found that the SAL exacerbated the dry period, suggesting that the different convective conditions at the east and west could have been the reason for western rain surpluses amidst high dust concentrations. With this, the guiding question is

What is the significance (contribution) of local convective forcing on rainfall in westernPuerto Rico?

1.2. Island-Scale Impacts on Rain

Within the constraints set by the large-scale conditions, local diurnal thermal and mechanical processes enhance dry (moist) convection and sensible (latent) heat fluxes in the island environment (Pielke et al., 2011). Several researchers have investigated these processes over select Caribbean Islands including Dominica (Minder et al., 2013; Nugent et al., 2014; Wang & Kirshbaum, 2015) via the Dominica Experiment (Smith et al., 2012), Barbados via the Barbados Oceanographic and Meteorological Experiment (Prospero & Carlson, 1972), and Puerto Rico with the Rain in Shallow Cumulus over the Ocean Experiment (Rauber et al., 2007). On the island of Puerto Rico, the Cordillera Central mountain range along its center (18.25 N), and the El Yunque rain forest on its eastern side (18.32 N, 65.78 W) orographically lift moist air over them (mechanical). In addition, intense convective storms most prevalent during the summer are triggered when trade winds and surface heating induced sea breezes converge (thermal) in the west during the afternoon hours (Jury et al., 2009).

The locations in Puerto Rico with the highest annual rainfall totals include high-elevation sites and the northwest, in proximity to westerly sea breeze flow—these conditions are in agreement with Krause and Flood (1997). Local convective processes therefore contribute to the island's rainfall climatology (Figure 2), attained from the parameter-elevation regressions on independent slopes model (Daly et al., 2002, 2003). Due to the high rainfall totals observable from the rainfall climatology, the wetter west compared to the east during the extreme drought of 2015, and unique thermal and mechanical convective conditions in the west, we focus our investigation on the region bounded from 17.9 N to 18.6 N and −67.3 W to −66.75 W.

Amidst the exceptional character of the transitioning (dry to wet) 2015–2016 period, during which an abnormally strong El Niño, positive winter NAO, and high regional dust concentrations occurred at the
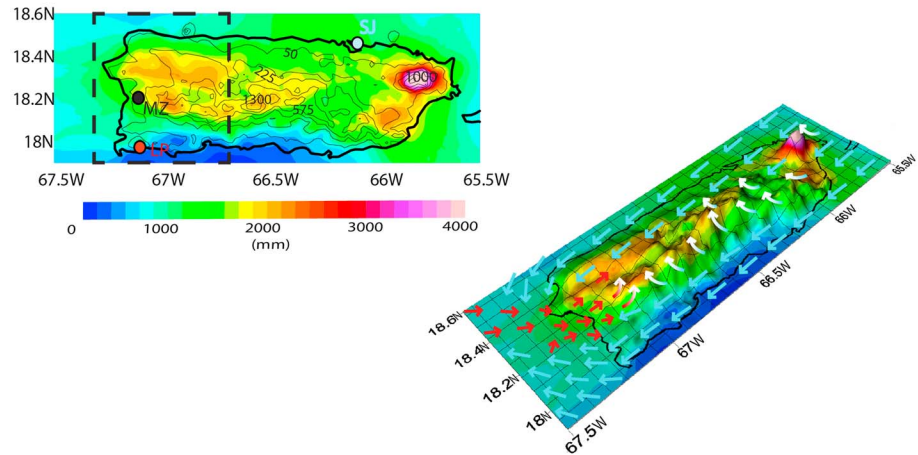
Figure 2. The 33-year (1963–1995) PRISM annual precipitation normals over the topography of Puerto Rico in 2D with topographic contour lines (left) and 3D (right). Circles indicate Mayaguez (MZ, black), La Parguera (LP, red), and San Juan (SJ, light blue). The dashed box shows the investigation area. Light blue arrows indicate the predominant winds; red arrows indicate surface heating induced sea breeze; and arrows with white tips (both red and blue) indicate convection.

outset, we are given the unique opportunity to improve understanding of the impacts of tropical island-scale processes on local rain events. This could lead to the improved characterization of tropical precipitation dynamics. A methodology describing the data and procedures will be presented in the next section, after which regional and local results will be presented. Lastly, this manuscript will close with conclusions.

2. Methodology

This study involved three components. The first is (a) the determination of the regional dust (July), rain accumulation (July), ENSO (July), and NAO (December–March) conditions between 1980 and 2016 (coinciding with the availability of dust data) for the region bounded by 100–55°W and 6–30°N. This allowed for comparison of conditions in 2015–2016 with other years during the period (section 2.1). The second component involved (b) a description of local rainfall conditions in Puerto Rico during 2015–2016 via characterization of locally enhanced western storms. Rain events occurring between 1 June 2015 and 31 July 2016 were characterized as light, moderate, or heavy using the 4 by 4-km Advanced Hydrologic Prediction Service (AHPS) total daily precipitation product, and the strength of the storms was determined (section 2.2). Lastly, the third component involved the (c) study of the impact of thermal and mechanical forcing on local convective storms that occurred during the Convection, Aerosol, and Synoptic-Effects in the Tropics (CAST) campaign (Hosannah et al., 2017) via the analysis of radiosonde, soil moisture, and aerosol data. This included topographic and coast proximity effects (section 2.3).

2.1. Large-Scale Data Sets and Pertinent Climate Indices

To assess how Caribbean moisture during 2015 and 2016 differed from other years during 1980–2016 and to ascertain how regional conditions changed from June 2015 to July 2016, a series of data sets and climate indices were studied. Variables of interest included monthly precipitable water (PW) from the National Center for Environmental Prediction (Kalnay et al., 1996) reanalysis product, monthly SST from the National Oceanic and Atmospheric Administration Optimum Interpolation Sea Surface Temperature (Reynolds et al., 2002) product, regional Climate Prediction Center Merged Analysis of Precipitation (Xie & Arkin, 1997) monthly precipitation data, and Modern-Era Retrospective analysis for Research and Applications version 2 (Gelaro et al., 2017) monthly dust mass concentrations. Meteosat-9 and Cloud-Aerosol Lidar and Infrared Pathfinder Satellite Observation satellite imagery were used for horizontal and vertical dust tracking.

Climate indices of interest included the December–March NAO, the July multivariate ENSO index (MEI), and the standard precipitation index (SPI). The MEI (Wolter & Timlin, 2011) was selected because it incorporates SLP, surface wind speed and direction, SST, surface air temperature, and total cloudiness fraction to determine ENSO strength. Positive MEI indicates anomalously dry conditions in the Caribbean. The SPI is an indicator of drought strength using precipitation only (Keyantash & Dracup, 2002; McKee et al., 1993), with negative values indicative of drier than usual conditions. MEI-precipitation, NAO-precipitation, and dust-precipitation correlations (Pearson's) were calculated for the 1980–2016 period. In addition, a hypothesis test was conducted to determine the statistical significance (95%) of the three data pairs. The appropriate null hypothesis in this case is that MEI, NAO, and Saharan dust do not linearly impact precipitation over the Caribbean region for the time period tested.

2.2. Determining Locally Enhanced Convective Events

The strategy for storm classification involved using the 4 by 4-km resolution AHPS 24-hr total accumulated precipitation product to calculate the precipitation area and intensity for each storm within the 427-day period. Storm durations were determined by studying hourly AHPS data. The AHPS observed precipitation product is attained via next generation radar estimates that are compared to and combined with rain gauge data and satellite precipitation estimates to produce a quality-controlled field (Seo, 1999). Step 1 involved determining the statistical distribution using terciles (33% and 66%) for rainfall events based on the precipitation accumulations. In order to determine the terciles, the maximum precipitation value for each storm was determined and arranged from lowest to highest. We then multiplied the tercile value by the number of storms plus 1 to attain the rank. If a storm event had a maximum precipitation total of less than 33 mm (33% quantile) in a 24-hr period (from 0800 the day of the storm to 0800 Atlantic Standard Time [AST] the day after) it was considered a light event. If a storm event had a maximum precipitation total between 33 and 87 mm (33–66% quantile), it was considered a moderate event. If a storm event had an average precipitation total above 87 mm it was considered a heavy event.

All rain events occurring within the region bounded by 17.9 N to 18.6 N and −67.3 W to −66.75 W were queried by size such that storms up to 15% of the western area were considered small, storms 15–25% were considered medium, and storms with above 25% coverage were considered large. The Storm Severity Index (SI, Waters, 2011), used to characterize storm degree, was determined for each storm. The SI is adapted via a graphical method that incorporates storm area, average rainfall over the area, and storm duration to ascertain the strength of a precipitation event. The SI emulates the rating of the Richter scale as used for earthquakes where a 5 denotes a light event that does little damage and flooding, a 7 causes extensive damage and flooding, and a 9 is disastrous and rare. To determine the SI for a 5-hr storm with an area of 260 km^2 and an average accumulation of 40 mm, a line is drawn from the average accumulation value on the left vertical axis to the storm duration on the right vertical axis (line 1). Line 2 is then drawn vertically upward from the storm area value on the bottom axis until it intersects with line 1. Lastly, line 3 is perpendicular to line 1 and is drawn from the intersection point of lines 1 and 2 to the secondary bottom axis, indicating an SI of 5.4.

Once the local storms were characterized, Step 2 involved study of atmospheric conditions via National Weather Service (NWS) weather maps, storm reports, and weather forecasts. Features of interest included (a) north-south oriented tropical waves characterized by fair weather to the west caused by upper (lower) level convergence (divergence) and active weather to the east caused by upper (lower) level divergence (convergence), (b) frontal banded precipitation, and (c) tropical cyclones identifiable by a low-level circulation rotating counterclockwise in the Northern Hemisphere. If the conditions were such that tropical waves were not immediately over or within 500 km to the west of Puerto Rico, no cyclones were within 1,000 km, and no severe thunderstorms occurred along a band exceeding the width of the island (60 km), the spatially localized event was classified as a locally enhanced convective event. Step 3 involved determination of the 1300 AST wind directions from the Finca Alzamora weather station (18.21 N, −67.16 W) for each rain event because substantial surface heating has occurred by this time, and sea breeze can develop. The Finca Alzamora station is 1.2 km from the west coast and 43 m above sea level, with no trees or buildings to obstruct wind flow. While surface roughness, heating, and terrain effects could possibly affect the sea breeze flow, we neglect these impacts as the distance from the coast is short. Lastly, Step 4 involved further analysis

of data collected during CAST (section 2.3) to assess local impacts on the formation and development of local convective storms.

2.3. CAST Monitoring of Western Puerto Rico

Between 2015 and 2016, Puerto Rico's observational network included 47 U.S. Geological Survey ground stations, a WSR-88D next generation radar, eight Natural Resources Conservation Service soil moisture sites, NWS radiosonde launches on the east (0800 and 2000 AST), and three AERONET Sunphotometers. Despite the rich observational network, there were observing gaps on the west (except for AERONET, which had two sites in the west and one in the northeast). To study local impacts on western storms, and to increase observational capabilities in western Puerto Rico, the CAST field experiment was conducted. The CAST measurement period was divided into four phases encompassing 22 June to 11 July 2015, 6–22 February 2016, 25 April to 7 May 2016, and 27 June to 12 July 2016. Building from the learnings of the aforementioned Caribbean observational campaigns (Dominica Experiment, Barbados Oceanographic and Meteorological Experiment, and Puerto RIco Dust Experiment), CAST allows for the analysis of locally measured variables to be studied along with large-scale data sets to investigate multiscale precipitation drivers. CAST instruments at the University of Puerto Rico at Mayaguez (18.21 N, 67.14 W) included EC-5 soil moisture sensors (Decagon), M10 radiosondes (Meteomodem), and a CL51 ceilometer (Vaisala, 910 nm). For more information on all the instruments employed during CAST, the reader is referred to http://cuerg.ccny.cuny.edu/cast. University of Puerto Rico at Mayaguez also contained a CIMEL Electronique 318A spectral radiometer (AERONET), as did Isla Magueyes, a small island off the southwestern coast of Puerto Rico (17.97°N, 67.04°W).

The soil moisture sensors measured volumetric water content, which was used to determine moisture availability. The Bowen ratio, the ratio of the sensible to latent heat flux, was calculated via the Geostationary Satellite-Puerto Rico Water and Energy Balance (GOES-PRWEB) algorithm (Harmsen et al., 2009) to estimate the amount of energy the land contributed to convective storm development. The algorithm utilizes an energy balance approach (Yunhao et al., 2001), estimated net radiation (Allen et al., 1998), and derived solar radiation (Diak et al., 1996; Gautier et al., 1980; Otkin et al., 2005). Any increase of the water content in the upper soil layer decreases Bowen ratio, increasing atmospheric water vapor content and the absorption of downward terrestrial radiation flux. As net radiation is enhanced in wet soil, increased total heat flux from the surface into the boundary layer occurs (Eltahir, 1998). Simultaneously, wet cooler surfaces are associated with reduced sensible heat flux and lower boundary layer depths. Enhanced surface heat flux into the boundary layer could produce large amounts of moist static energy, and consequently, localized convective storms have been shown to be sensitive to the distribution of boundary layer moist static energy (Williams & Renno, 1993).

The ceilometer measures vertical visibility at 10-m resolution via backscatter measurements and detects up to three cloud layers simultaneously. The spectral radiometer measures the Sun and sky radiances at fixed wavelengths (340, 380, 440, 500, 675, 870, 1020, and at some sites 1,620 nm) within the visible and near-infrared spectrum. Cloud-screened aerosol optical thickness (AOT) and Ängstrom exponent, which represent total aerosol column average within the atmosphere, are attainable from radiometer measurements (AERONET). Dust intensity over Puerto Rico during and outside of CAST was determined from ceilometer backscatter, column-integrated AERONET AOT at 340, 500, and 1,020 nm to detect a range of particle sizes, and the Ängstrom exponent (Eck et al., 2012).

The radiosondes provide air and dew point temperatures, PW content, relative humidity, and wind speed and direction. The data were used to calculate the convective available potential energy (CAPE), lifted index (LI), humidity index (HI), and the bulk Richardson number (BRN). The LI measures atmospheric instability by calculating the temperature air near the ground would have if it were lifted adiabatically to 500 mb and compared to the actual temperature at 500 mb (Johns & Doswell, 1992). The more negative the LI, the more unstable the environment and the stronger convective updrafts are likely to be. CAPE is another indicator of local stability/instability and reflects the amount of energy an air parcel would have if it were lifted from the level of free convection to the equilibrium level. CAPE values above 2.5 kJ/kg suggest severe instability and the likelihood of intense rain events. The HI is calculated by summing the differences between the parcel and dew point temperatures at 500, 700, and 850 mb and measures instability and convective potential (Litynska et al., 1976). Values above 50 indicate low moisture and
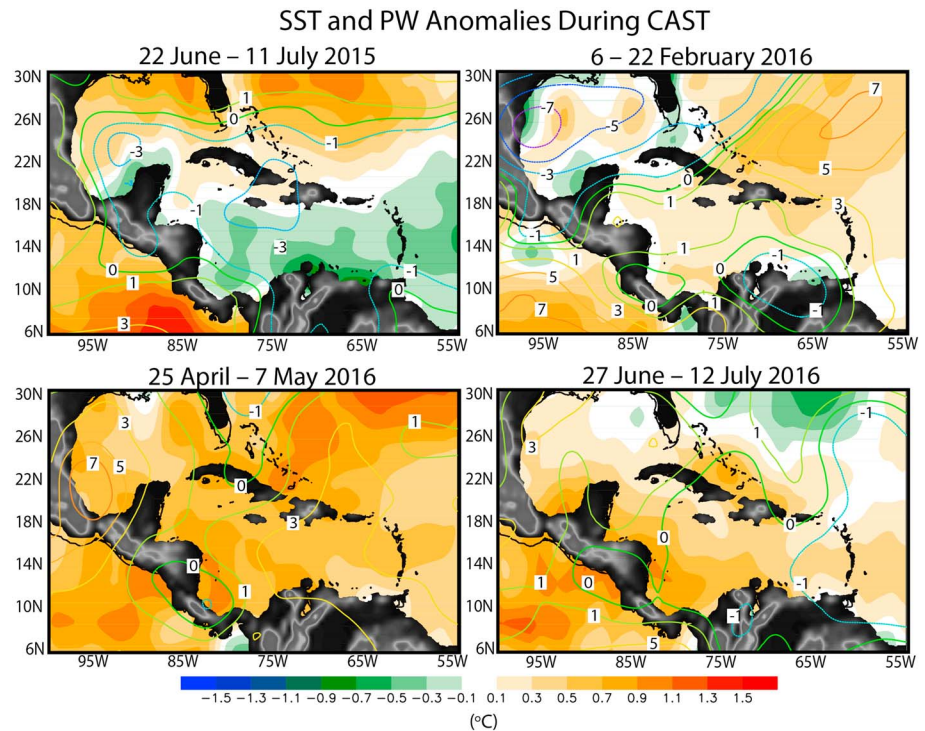
Figure 3. SST anomalies (shaded, °C) and PW anomalies (contours, kg/m^2) for 22 June to 11 July 2015, 6–22 February 2016, 25 April to 7 May 2016, and 27 June to 12 July 2016. PW = precipitable water; SST = sea surface temperature.

weak instability potential, values between 30 and 50 are moderate, and values below 30 indicate high moisture and strong instability potential. Finally, the BRN is a nondimensional ratio of the buoyant force (CAPE) to the vertical wind shear and provides a proxy for convective strength versus mitigation (Hart & Korotky, 1991). Values less than 45 support supercell convection, while values above 45 support multicell or ordinary cell convection (Weisman & Klemp, 1986).

3. Results

3.1.1. Regional Conditions

A time series of MEI, NAO, normalized Saharan dust mass concentration (kg/m^3), and normalized precipitation (mm) from 1980 to 2016 informed of the average regional moisture conditions. Positive NAO values (1.7) were observed during the 2014–2015 winter with 2015 being the strongest El Niño onset year since 1997, co-occurring with negative SST anomalies (Figure 3) and the highest dust concentration during the 37-year period. These conditions led to a drier-than-usual summer 2015, confirmed by negative Climate Prediction Center Merged Analysis of Precipitation precipitation anomalies. Precipitation correlations with MEI, NAO, and Saharan dust for 1980–2016 show low to moderate correlations that are not statistically significant (−0.14, −0.42, and 0.1, respectively). We therefore cannot reject the null hypothesis that NAO, MEI, and Saharan dust do not linearly impact Caribbean rainfall for these data sets during 1980–2016. We also noted a decreasing trend in dust mass concentration from 1980 to 1990, while an increasing trend is observed from 1991 to 2016. Despite the general lack of significance between MEI, NAO, and dust with precipitation, local storms in Puerto Rico are still impacted by these large-scale variables as they govern moisture conditions in the region.

3.1.2. Conditions During CAST Phases

The strong inverse relationship between the MEI and SPI in June–July 2015 corroborates the extremely dry summer 2015 conditions (Table 1). Figure 3 shows negative PW and negative SST anomalies in the Caribbean Sea, two countervailing factors for precipitation production. During the dry season (December to February), SPI and MEI relaxed, NAO reduced compared to 2014–2015 winter, available PW increased along the island chain, east of Cuba, and SSTs increased in the Caribbean Sea. In the spring (March to

Table 1
Regional Indices and Surface-Atmospheric Variables

Variable	June–July 2015	December 2015 to February 2016	March–May 2016	June–July 2016
MEI	2	2.1	1.6	0.7
SPI	−3	−2 to 0.5	−0.5 to 1.5	−2 to 2
NAO	−1.1	1.3	0.1	1.1
SST	−0.1 to −1	0.1 to 0.7	0.4 to 1	0.1 to 1.1
PW	−1 to −3	1 to 3	3	−1 to 0

Note. PW = precipitable water; MEI = multivariate ENSO index; SPI = standard precipitation index; NAO = North Atlantic Oscillation; SST = sea surface temperature; ENSO = El Niño–Southern Oscillation.

May 2016) SPI and MEI were more favorable for rainfall production, as NAO was near neutral, and SSTs as well as PW increased over nearly the entire Caribbean. This period was characterized by predominately southeasterly winds and higher clouds (from radiosonde data, not shown). From June into July 2016, conditions increasingly favored rainfall as positive SST anomalies, and near climatological PW values occurred over the Caribbean Sea.

3.2. Local Conditions

Negative precipitation anomalies occurred at over 70% of Puerto Rico in June 2015 (Figure 4a), with a smaller positive precipitation anomaly in the northwestern quadrant. There were negative anomalies for over 85% of the island during July 2015 (Figure 4b). Between 22 June and 11 July 2015, rainfall occurred on 27% of days. Dust intensity peaked in July, with an average AOT of 0.293. The drought conditions began to dissipate after July 2015, and October was the wettest month between August and November with positive precipitation anomalies (+100 mm) at over 75% of the island (Figures 4c–4f). There were frequent island-wide storms, indicative of large-scale atmospheric contributions. December 2015 was drier than usual except in the northwest and east (Figure 4g). In January 2016 a band of positive precipitation anomalies (50–125 mm) over the southern half of the island (17.9–18.2°N) was detected (Figure 4h), spreading during February 2016 (Figure 4i), when positive precipitation anomalies were observed over a large portion of the northwest quadrant, along the west coast, in the south-central coastal area, over El Yunque, and at the southeast coastal areas. The average AOT diminished to 0.063, reflecting minimal dust. Precipitation occurred on over 60% of CAST campaign days. The northwest exhibits the highest negative anomalies in March 2016 (Figure 4j). This condition changes significantly in April 2016 with positive rainfall anomalies along the northern, southern, and eastern coasts (Figure 4k). Most of the negative anomalies during April 2016 were along the northern slopes of the Cordillera Central. During May 2016, negative anomalies increased along the center and spread to the southern coast and the northeast quadrant (Figure 4l). The negligible dust condition continues (AOT of 0.065) until June 2016, when the average local AOT in Puerto Rico increased to 0.251.

Ceilometer backscatter during CAST (Figure 5) corroborates these seasonal AOT variations, showing higher backscatter intensities during June–July (2015 and 2016) than in February and April–May of 2016. Despite an abnormally dry May 2016 (65.5% less precipitation than the climatological value for over 80% of Puerto Rico), conditions during the summer of 2016 were in stark contrast to summer 2015, with wetter conditions (June and July rain totals were 7% lower and 8.5% higher, respectively, than climatological means in Puerto Rico). June 2016 was characterized by
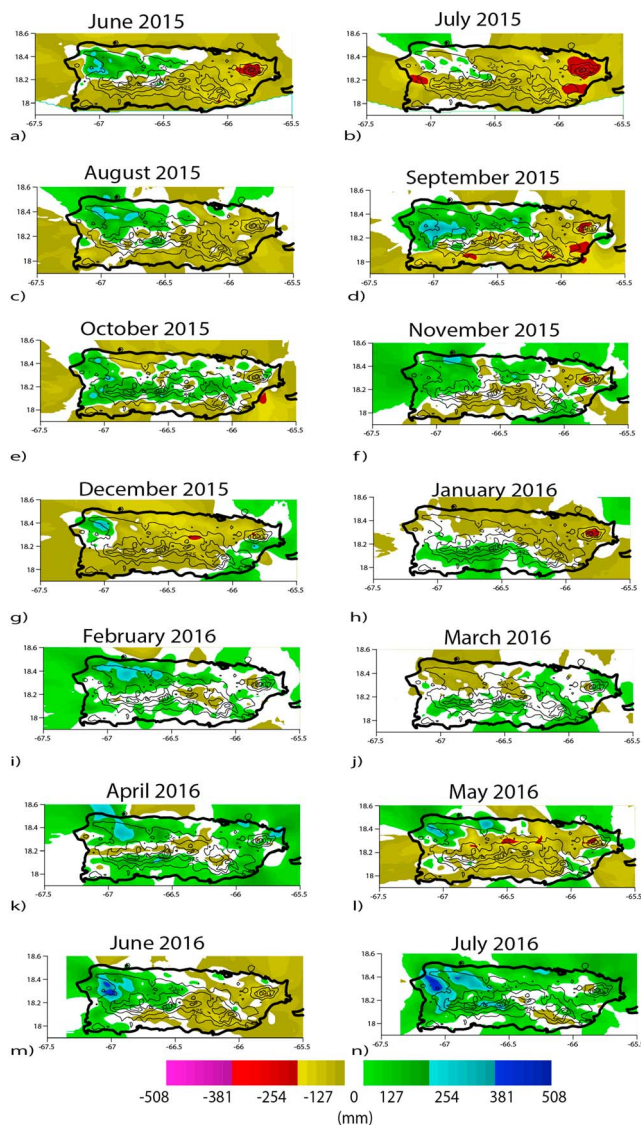

Figure 4. AHPS total monthly precipitation anomalies (shaded) from June 2015 to July 2016 and select topographic contours (lines). AHPS = Advanced Hydrologic Prediction Service; PW = precipitable water; SST = sea surface temperature; CAST = Convection, Aerosol, and Synoptic-Effects in the Tropics.
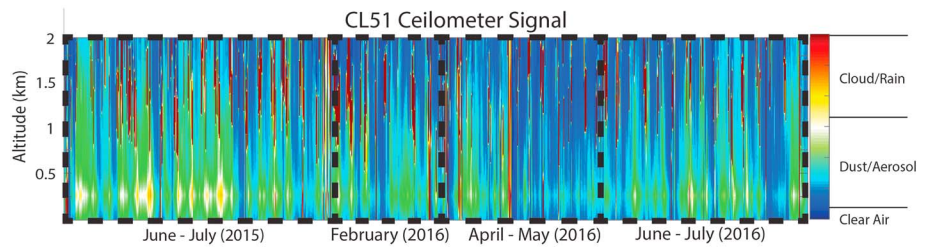
Figure 5. CL51 backscatter intensity measured during CAST phases. CAST = Convection, Aerosol, and Synoptic-Effects in the Tropics.

positive rainfall anomalies on the western half of the island (Figure 4 m) and 90% of the island experienced positive rainfall anomalies in July 2016 (Figure 4n). During the 27 June to 12 July 2016 CAST period, rain occurred on all days. Winds were predominately easterly, with strong westerly sea breezes during the afternoon hours.

The Cordillera Central serves as a natural boundary that promoted sharp gradients in precipitation anomalies for all months except October and December of 2015. Puerto Rico exhibits positive anomalies to the northwest and negative anomalies to the south and east, consistent with sea breeze convergence. During April 2016, the leeward (northern) side of the mountain range is subjected to negative anomalies induced by the rain shadow effect. Precipitation deficits expand to the south and east as the season extends and the wind changes in May. Further wind changes caused western convergence enhancement during June, followed by island-wide enhancement in July 2016 with the highest positive anomalies in the northwest, along the central mountains, and in the San Juan metropolitan area.
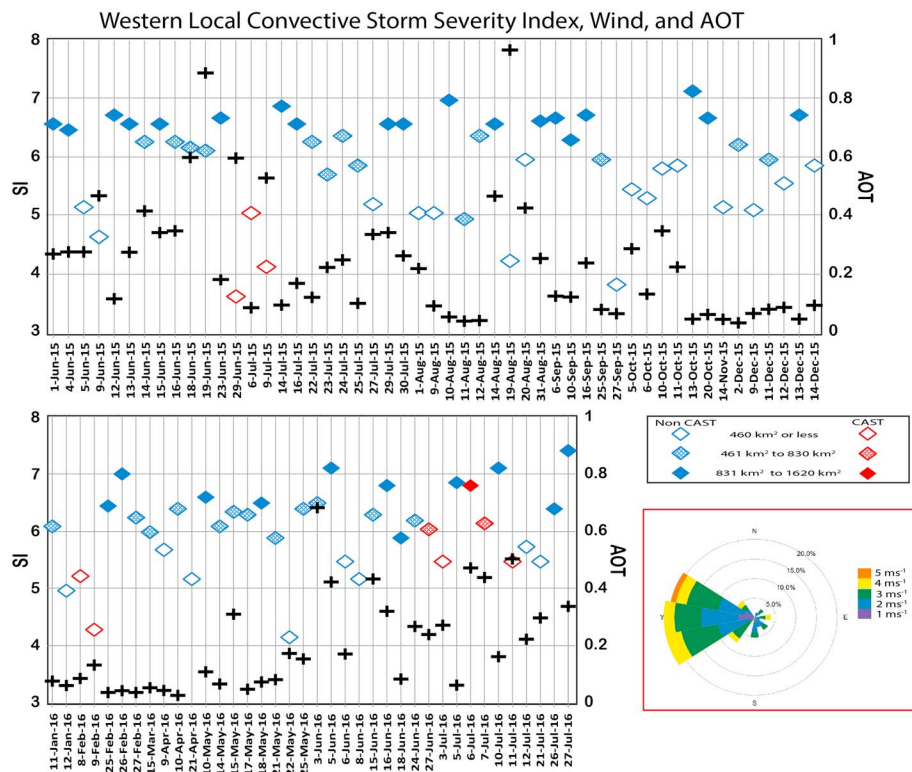

Figure 6. The AOT (crosses) and SI for localized storms during (red diamonds) and outside of (blue diamonds) CAST with areas less than 460 km^2 (open diamonds), between 461 and 830 km^2 (gridded diamonds), and between 831 and 1620 km^2 (filled diamonds). The wind rose (bottom right) shows the 1300 AST wind speeds and directions at the Finca Alzamora station. CAST = Convection, Aerosol, and Synoptic-Effects in the Tropics; SI = Severity Index; AOT = aerosol optical thickness; AST = Atlantic Standard Time.
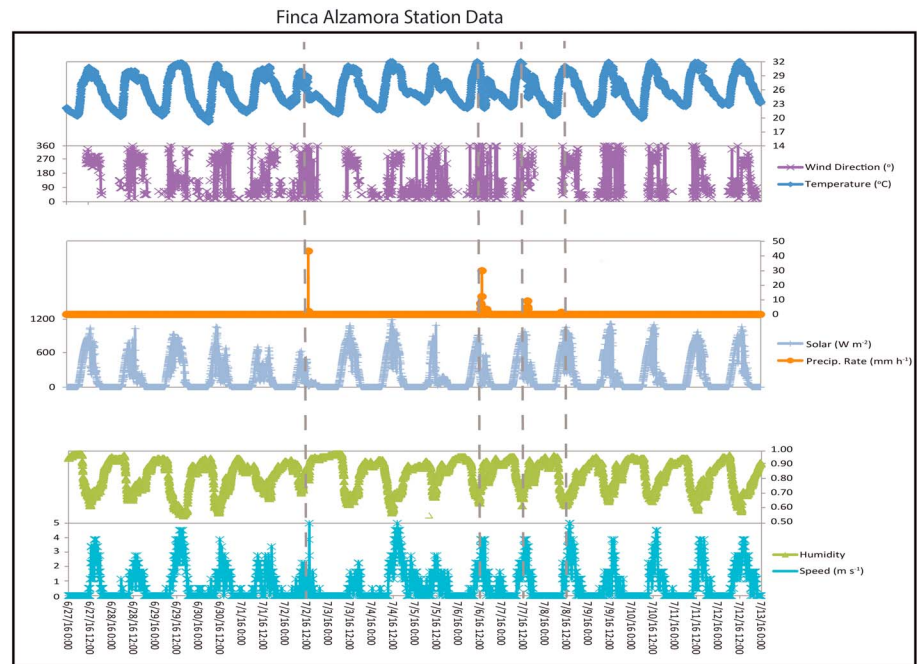
Figure 7. Subhourly temperature (dark blue), wind direction (purple) and speed (aqua), humidity (light green), solar radiation (light purple), and precipitation rate (orange) at the Finca Alzamora station from 27 June to 12 July 2016. Dashed lines depict 1200 AST on days when the station observed rainfall. AST = Atlantic Standard Time.

3.3. Local Convective Storms

Out of 322 rain events occurring over Puerto Rico between 1 June 2015 and 31 July 2016, 89 were found to have local western enhancement, and 10 events occurred during CAST phases. These 89 events were mostly afternoon convective storms and ocurred without the immediate influence of tropical waves or frontal passage. Fifty-three of the storms (60%) occurred during the summer months. The AOT (for 86 days) and SI for all 89 storms separated by storm size are shown in Figure 6. Sixty-seven of the 86 storms with AOT data available (AERONET) were coincident with AOT lower than 0.3. Storm area tended to decrease with AOT increases, yet as the correlation between SI and AOT varied for large (0.096), medium (0.261), and small (-0.282) storms, other factors must play a role in the enhancement or impedance of these storms. As an example, the prevalence of thermally induced sea breeze is indicated by the 1300 AST winds for all 89 events, which show the dominance of southwesterly-northwesterly wind conditions 83% of the time (Figure 6, bottom right).

As most of the local storms occurred during the summer afternoon hours, we present a sample of subhourly temperature, wind speed and direction, solar flux, humidity, and precipitation rate data between 27 June 2016 and 12 July 2016 from the Finca Alzamora station (Figure 7). The air temperature peaks (30–32 °C) near 1200 AST, coinciding with the maximum solar radiation (600–1,200 W/m^2), minimum humidity (55–70%), and westerly winds that peak in strength (2–5 m/s) at the same time. The storms normally begin within a few hours of these peaks. The minimum nighttime temperatures ranged from 18 to 23 °C. These plots provide an example of the diurnal cycle in the west and point to characteristic thermal forcing conditions.

3.4. Analysis of CAST Storms

To show how the local CAST events compare to nonlocalized rain events (over 40% of the western area or events with multiple cells) and dry events (no rainfall anywhere on the island), we queried all 42 days on which CAST radiosondes were launched, with seven dry events, 25 nonlocalized rain events, and the 10 local western storms (Table 2). The local CAST storms on average exhibit the highest CAPE (2.3 kJ/kg) when compared to averages for dry (1.49 kJ/kg) and nonlocalized (2.04 kJ/kg) events. AOT is highest for dry and local rain events (0.3–0.36), and are 2 to 3 times higher than the nonlocalized cases (0.1–0.17). The LI is deeply

Table 2
Stability Indices, SI, AOT, and PW for Local CAST Storms (N/A Means Not Applicable)

Storm	CAPE (kJ/kg)	BRN	LI	SI	HI	AOT (1,020 nm)	AOT (500 nm)	AOT (340 nm)	PW (mm)
6/29/2015	3.734	28	−7	3.7	35	0.555	0.605	0.599	47.7
7/6/2015	2.097	68	−3	5.1	40	0.068	0.102	0.104	41.9
7/9/2015	2.838	848	−7	4.2	39	0.458	0.530	0.458	44.1
2/8/2016	0.795	193	0	5.25	34	0.124	0.177	0.217	43.7
2/9/2016	0.962	231	1	4.33	45	0.093	0.144	0.18	43.7
6/27/2016	2.839	391	−6	6.05	17	0.211	0.220	0.234	53.7
7/3/2016	1.35	51	−3	5.5	46	0.25	0.281	0.292	47.7
7/6/2016	2.342	84	−6	6.8	5	0.434	0.478	0.478	63.8
7/7/2016	2.618	81	−4	6.15	35	0.39	0.445	0.459	55.2
7/11/2016	3.418	208	−7	5.5	37	0.471	0.509	0.515	54.6
Average CAST local storms	2.3	218.3	−4.2	5.2	33.3	0.305	0.341	0.343	49.6
Average of nonrain days	1.49	71.9	−2.6	N/A	33.1	0.301	0.354	0.359	43.3
Average of nonlocal rain days	2.04	339.1	−3.8	5.7	27.3	0.102	0.143	0.167	51.3

Note. CAPE = convective available potential energy; CAST = Convection, Aerosol, and Synoptic-Effects in the Tropics; BRN = bulk Richardson number; LI = lifted index; HI = humidity index; SI = Severity Index; AOT = aerosol optical thickness; PW = precipitable water.

negative for the local storms (−4.2), and 162 and 111% lower than the dry (−2.6) and nonlocal storms (−3.8), respectively. Expectedly, the average PW for nonrain events is the lowest, with a value of 43.3 mm, and local (nonlocal) events follow with 49.6 (51.3) mm. BRN follows this trend with 71.9, 218.3, and 339.1. Lastly, the average SI for nonlocalized events is 110% (5.7) that of the local storms (5.2) as a result of larger storm areas.

Local events on average exhibit the highest CAPE and lowest LI values amidst the second highest PW availability, which suggests high local instability, and buoyant moist air masses to enhance very localized (small spatial area, hence the lower SI index) thermally forced storm events even in high AOT scenarios. Nonlocal events on average exhibit higher precipitable water, low AOT, lower CAPE (although still moderately high), and less negative LI. Nonrain days were characterized by low CAPE, low PW, higher LI, and high AOT.

Out of the 10 localized events occurring during the CAST field campaigns, eight occurred during June and July of 2015 and 2016, and two occurred during February of 2016. The total 24-hr accumulated precipitation for each storm (AHPS) is shown in Figure 8. The summer 2015 (29 June and 6 and 9 July) and dry season 2016 (8–9 February) localized CAST storms were lower in intensity and exhibited less spatial coverage than the summer 2016 storms (27 June, 3, 6, 7, and 11 July). The eight summer storms had coverage within 20 km of the west coast, whereas the two dry season events produced rain farther inland, concentrated along the northern slopes of the mountainous Cordillera Central terrain, attributed to mechanical forcing.

Daily and average (calculated for the 22 June to 11 July 2015, 6–22 February 2016, 27 June to 12 July 2016 periods) Bowen ratios calculated from GOES-PRWEB at three locations along 18.201 N (66, 66.75, and 67.15°W) in Table 3 show that the sensible heat release inland (66°W) was 3.8–7.5 times higher than the latent heat release during the three summer 2015 localized CAST storms, reducing to a factor of 2.25 during the two dry season storms, and further for the summer 2016 storms to a factor of 1.25–2. Values at 66.75°W are almost half the respective averages during the 3 periods (for which storms occurred during CAST—summer 2015, February 2016, and summer 2016) for 8 out of 10 events. Lastly, the values near the coast (67.15 W) are higher than the 22 June to 11 July 2015 average by a factor of 2, and higher than the 27 June to 12 July 2016 average by 1.5, yet values during the 2016 dry season storms (8–9 February 2016) are 2.8 times less than the 6–22 February 2016 average. As any increase of the water content in the upper soil layer decreases Bowen ratio, the highest values for events occurring during the extreme summer drought of 2015 inland (66°W) are expected. Conversely, as the soil is wetter during summer 2016, the large decrease in Bowen ratio at the same location is also expected. The wetter soil should expend more latent heat from the surface, increasing moist static energy. The accompanying cooler surface associated with increased soil dampness for the February and summer 2016 storms produces smaller (higher) sensible (latent) heat fluxes and releases more moisture into the atmosphere. The *differences* between the Bowen ratio for the three periods reduce closer to the coast (66.75 and 67.15°W), although the lowest Bowen ratio values occur at the trailing western edge of the Cordillera Central (66.75°W), a location subjected to both mechanical and thermal convective forcings.
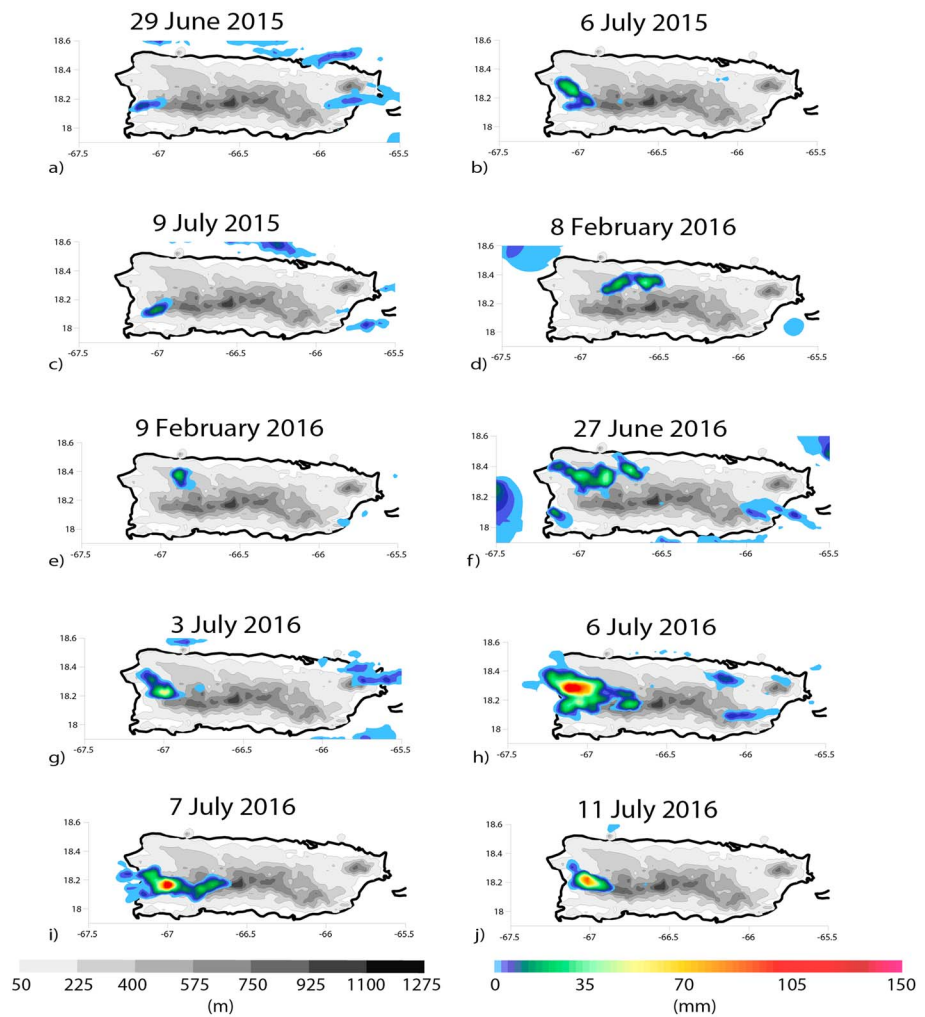
Figure 8. AHPS total precipitation (color shading) over topography (grayscale shading) for the localized western events occurring during CAST. AHPS = Advanced Hydrologic Prediction Service; CAST = Convection, Aerosol, and Synoptic-Effects in the Tropics.

These findings support the increased release of moist static energy near 66.75 W and near the coast, as well as the soil moisture-precipitation feedback.

Radiosonde data for the 10 local CAST storms (Figure 9) show low-level flow (975 mb) from the west (29 June 2015, 27 June 2016, and 3 July 2016), southwest (6 July 2015 and 6 July 2016), or northwest (9 February 2016 and 11 July 2016). This indicates sea breeze that interacts with the prevailing easterly flow (corroborated by NWS wind forecasts, National Center for Environmental Prediction reanalysis wind

Table 3
Bowen Ratio Along 18.21°N for 10 CAST Storms and Seasonal Averages During Summer 2015, Dry Season 2016, and Summer 2016

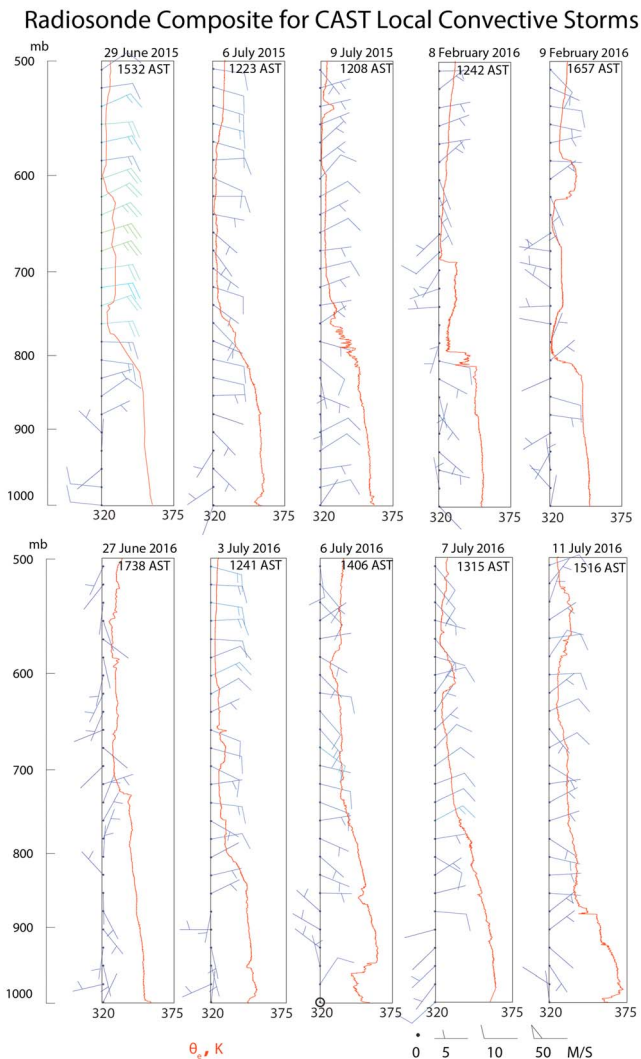|	29 Jun 2015	6 Jul 2015	9 Jul 2015	8 Feb 2016	9 Feb 2016	27 Jun 2016	3 Jul 2016	6 Jul 2016	7 Jul 2016	11 Jul 2016
67.15°W	<u>2.07</u>	<u>1.76</u>	2.09	0.58	0.60	0.82	1.53	1.50	1.55	1.65
66.75°W	0.66	0.49	0.99	0.99	0.92	0.88	1.29	1.16	0.78	0.58
66°W	7.63	3.78	4.16	2.19	2.13	1.36	1.92	1.38	1.15	1.40
Average 67.15°W	1.69	1.69	1.69	1.72	1.72	1.30	1.30	1.30	1.30	1.30
Average 66.75°W	0.85	0.85	0.85	1.51	1.51	0.96	0.96	0.96	0.96	0.96
Average 66°W	5.81	5.81	5.81	1.96	1.96	1.38	1.38	0.96	1.38	1.38

Radiosonde Composite for CAST Local Convective Storms

Figure 9. Radiosonde composite with horizontal winds (barbs) and θ_e (red plots) for the 10 local convective storms during CAST. CAST = Convection, Aerosol, and Synoptic-Effects in the Tropics.

products, North American Mesoscale [NAM] model data (Environmental Modeling Center/National Centers for Environmental Prediction/ National Weather Service/NOAA/U.S. Department of Commerce, 2015), and weather stations at coastal and inland locations). In addition, while unable to simultaneously show both the prevailing easterly winds and the westerly sea breeze at a particular height from the radiosonde soundings alone, predominately easterly flow is observed above 850 mb. The stronger events (SI of 5.5 or higher) exhibit increased CAPE and PW as well as reduced BRN, LI, and HI (6, 7, and 11 July 2016). Relative humidity for dry season events (8 and 9 February 2016) was above 85% up to the 700-mb level but was markedly drier than the other events above 700 mb, whereas summer events exhibited a dry layer between 800 and 400 mb (not shown) attributed to the intensely dry and frequent SAL episodes (Raman et al., 2002).

Plots of the equivalent potential temperature (θ_e) for the dry season events (Figure 9) indicate near-neutral layers from the surface to 800 mb transitioning sharply to unstable layers between 800 and 770 mb, and near-neutral/stable layers aloft except at three levels where unstable air is present (670 mb on 8 February, 650 and 580 mb on 9 February). In contrast, aside from the varying near-surface θ_e conditions, the summer events generally have less variability in stability and show thicker unstable layers (950–600 mb), with stable layers aloft.

Note that all radiosondes were launched near the west coast, and the stable LI and CAPE values for 8 and 9 February 2016 are corroborated by the lack of precipitation near the west coast. The radiosondes launched on these two dates show northerly winds near 975 mb for both events; however, there is limited meteorological data to support the influence of mechanical forcing on storm production aside from the actual locations of the storms on the northern slopes of the Cordillera Central. While Caribbean Integrated Coastal Ocean Observing System (www.caricoos. org) wind data at Rincón (67.27 W, 18.30 N) corroborates the influence of northerly winds at the northwest of the island, the site is 60–80 km west of these inland storms.

Despite moderate to high CAPE during summer 2015 events, lower precipitation accumulations are recorded. With a CAPE of 3.734 kJ/kg, a LI of −7, and a BRN o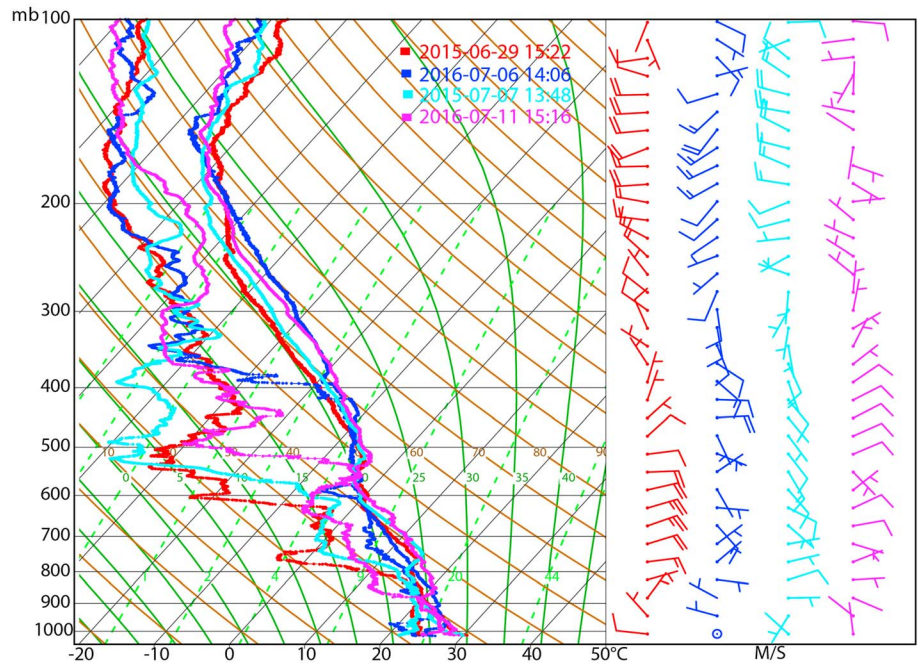f 28, the 29 June 2015 storm had the ingredients of a strong event; however, low PW (47.7 mm) compounded with intense dust (AOT ranging from 0.555 to 0.606) may have suppressed effective production of precipitation. Although the 29 June 2015 event supports the narrative of reduced precipitation coinciding with increased dust concentrations during June and July (revisit Figure 1), intense storm events during CAST did however occur under high AOT conditions (6, 7, and 11 July 2016). In these instances, local convective processes produced an unstable condition via moderate to severe CAPE (2.342 to 3.418 kJ/kg) and negative LI (−4 to −7) in the presence of moister air (PW above 54 mm) notwithstanding the rainfall mitigation effects of increased dust (AOT ranging from 0.434 to 0.515). Skew-T plots for these four high AOT events (29 June 2015, 6, 7, and 11 July 2016) are shown in Figure 10, indicating a saturated atmosphere between the surface and 400 mb during 6 July 2016, saturated conditions between the surface and 750 mb with the parcel rising along a dry adiabat (40 °C) from 750 to 600 mb on 7 July 2016, and saturated conditions between the surface and 850 mb with a pocket of drier air between 850 and 600 mb. The 29 June 2015 event exhibits a similar temperature profile to the 7 July 2016 storm with lower dew point temperatures in the low atmosphere to midatmosphere and shows a drier environment. These soundings also show possible convective capping due to dust for these days, identifiable by temperature inversions in the low (below 850 mb) and middle (between 500 and 600 mb) levels. Despite the inversions, parcel buoyancy was enough to produce intense storms on days with adequate moisture (6, 7, and 11 July 2016).

Figure 10. Radiosonde soundings for 29 June 2015 (red), 6 July 2016 (blue), 7 July 2016 (cyan), and 11 July 2016 (magenta). Brown gridlines denote dry adiabats (°C), solid green gridlines indicate saturation adiabats (°C), and dashed light-green gridlines indicate saturation mixing ratio lines (g/kg).
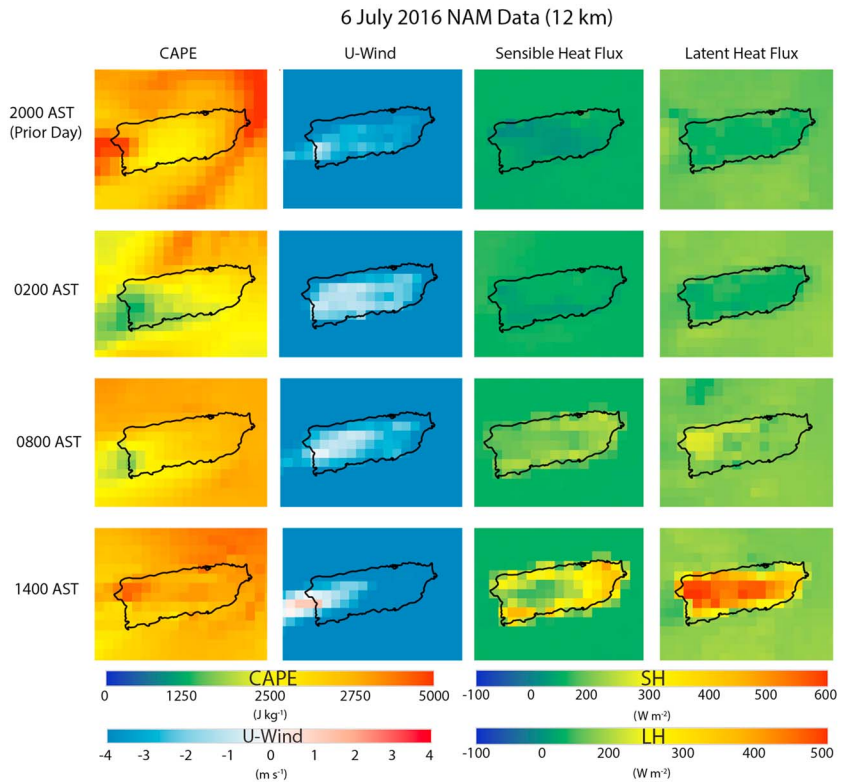

Figure 11. NAM 12 km CAPE, U-winds, sensible heat flux, and latent heat flux for 6 July 2016 at 2000, 0200, 0800, and 1400 AST. AST = Atlantic Standard Time; CAPE = convective available potential energy; NAM = North American Mesoscale.

Six-hourly NAM data (2000 AST the day prior to rain events, and 0200, 0800, and 1400 AST the day of rain events) for one of the high AOT cases (6 July 2016) validate that CAPE is at a minimum during morning hours, increasing in the afternoon and evening hours (Figure 11). While CAPE increases island wide throughout the day, the west exhibits the highest values. The Cordillera Central also shows moderate CAPE despite there being no rainfall at the eastern edge. Surface U-winds during the afternoon hours show sea breeze easterly convergence at the west coast, fueling convection at this location. Sensible heat (SH) release is at a minimum during the nighttime and early morning hours, rapidly increasing in the east, south, and north in the midmorning and afternoon hours. While latent heat (LH) flux is also at a minimum during the nighttime and early morning hours, the LH flux increases rapidly in the west and along the Cordillera Central between the midmorning and afternoon hours, opposite to the SH pattern. Results are similar for the other three days (29 June 2015, 7, and 11 July 2016, not shown). These results corroborate GOES PRWEB Bowen ratio calculations.

4. Summary

The goal of this work was to assess the impacts of tropical island processes on local convective storm production on a Caribbean island. A regional analysis (bounded by 100–55 W and 6–30 N) showed that MEI, NAO, and Saharan dust do not *linearly* impact rainfall in the Caribbean for the 1980–2016 period. Despite the lack of statistical significance, the positive NAO for the winter preceding the strong El Niño and the strong El Niño itself reduced available PW and SSTs during the summer of 2015. In addition, higher dust concentrations caused convective capping—reducing both humidity and the efficiency of cloud droplet growth mechanisms over the Caribbean region, including Puerto Rico.

Out of 322 rain events occurring over Puerto Rico from 1 June 2015 to 31 July 2016, 89 were found to be locally enhanced western convective storms, 53 of which occurred during the summer months. Dry conditions during 2015 transitioned to wetter conditions in 2016 as more local and intense storms occurred in Puerto Rico during 2016. The wetter western Puerto Rico is primarily attributed to the robust regional atmospheric conditions, which provided the local thermal and mechanical convective processes with the necessary moisture to enhance rainfall production. After the 89 local storms were characterized by size, duration, and rain totals (SI), an analysis of the local wind speed and direction uncovered strong afternoon southwesterly, westerly, or northwesterly wind conditions (sea breeze) for 83% of storms. While 75% of the storms were coincident with AOT values lower than 0.3, correlations between SI and AOT were low, with values of 0.096, 0.261, and −0.282 for large, medium, and small storms, respectively. This suggests that aerosol/dust alone cannot explain local precipitation modification, and that other variables should be considered to better understand the local contributions.

Ten of the 89 local convective storms occurred during the CAST campaign, with eight summer storms occurring within 20 km of the western coast, attributed to thermally induced sea breeze convergence, and two dry season storms occurred farther inland over the windward mountain slopes, attributed to mechanically forced orographic uplift. These storms exhibited a high incidence of low level westerly, northwesterly, or southwesterly flow. The most severe storms (SI above 5.5) occurred with PW above 50 mm, negative LI values (−4 to −7), and CAPE above 2.3 kJ/kg. Although increased dust concentrations can suppress droplet growth and cap convection, three of the most severe CAST rain events (6, 7, and 11 July 2016) occurred under moderate to heavy dust conditions (AOT above 0.4). In these cases, the storm mitigation effects of the dust (Rosenfeld et al., 2001) were likely attenuated by strong localized thermal and mechanical forcings (Jury & Chiao, 2013; Watson et al., 2015) in the presence of moist air.

Bowen ratios in western Puerto Rico showed that the highest values ocurred inland during the summer 2015 events. During summer 2016 the wetter environment led to a 73% reduction in the Bowen ratio compared to summer 2015. The differences between the Bowen ratio for the three periods reduce closer to the coast, although the lowest Bowen ratio values occur at the western edge of the Cordillera Central mountains, suggesting that local processes near the coast fuel the soil moisture-precipitation feedback (Eltahir, 1998). This is further supported by the analysis of NAM data, which showed sensible heat highs in the east, south, and north, and latent heat highs in the west and over the Cordillera Central mountain range. The west also exhibits the highest CAPE values and sea breeze easterly convergence during the afternoon hours.

The conclusions of this study are (1) one variable is not adequate to explain precipitation surpluses and deficits over the Caribbean region and Puerto Rico, rather precipitation totals reflect the collective effect of multiple processes and variables, (2) the west and high-elevation locations across the island are convective hot spots over which local thermal and mechanical forcings increased CAPE and latent heat release, resulting in the rapid ascension of buoyant moist air, and (3) even in the case of strong regional-scale drought conditions, local convective forcings enhance storm production and lead to surpluses at key positions across the island, particularly on the windward side of the mountains, and near the west coast.

As the aim of this study is to further our understanding of island scale impacts on rainfall, the continuous improvement of observational networks in the island environment remains a necessity. Even before the landscape of Puerto Rico was damaged by Hurricanes Irma and Maria in September 2017, meteorological stations at the peaks and along the slopes of Puerto Rico's mountain ranges were limited in number and measurement capability. The current lack of adequate sensors in the interior makes the analysis of inland storms close to mountains (such as the 8–9 February 2016 events) difficult. Despite the lack of mountain sites, additional sensors employed during the CAST campaign began to address some of the western spatial coverage issues; however, since Hurricane Maria severely damaged much of the island-wide observational infrastructure (non-CAST), the capabilities for studying local weather impacts have been hampered. Careful strategic planning is necessary to effectively study local surface atmospheric convective processes not only across the varying landscape of Puerto Rico but also for other coastal tropical environments where local thermal and mechanical convective processes contribute to surface-atmospheric interactions, producing the necessary precipitation for the survival of the inhabitants and sensitive ecosystems.

References

Allen, R. G., Pereira, L. S., Raes, D., & Smith, M. (1998). *Crop evapotranspiration guidelines for computing crop water requirements. FAO Irrigation and Drainage Paper 56* (p. 300). Rome: Food and Agriculture Organization of the United Nations.

Angeles, M. E., González, J. E., Ramírez-Beltrán, N. D., Tepley, C. A., & Comarazamy, D. E. (2010). Origins of the Caribbean rainfall bimodal behavior. *Journal of Geophysical Research*, *115*, D11106. https://doi.org/10.1029/2009JD012990

Birgmark, D., (2014). El Niño-Southern Oscillation and North Atlantic Oscillation induced sea surface temperature variability in the Caribbean Sea, Master's Thesis, University of Gothenburg, Department of Earth Sciences. 29 pp, https://gvc.gu.se/digitalAssets/1503/1503953_b830.pdf

Burpee, R. W. (1972). The origin and structure of easterly waves in the lower troposphere of North Africa. *Journal of the Atmospheric Sciences*, *29*(1), 77–90. https://doi.org/10.1175/1520-0469(1972)029<0077:TOASOE>2.0.CO;2

Carlson, T. N., & Prospero, J. M. (1972). The large-scale movement of Saharan air outbreaks over the northern equatorial Atlantic. *Journal of Applied Meteorology*, *11*(2), 283–297. https://doi.org/10.1175/1520-0450(1972)011<0283:TLSMOS>2.0.CO;2

Coto, D. (2015a). Caribbean braces for worsening drought as dry season nears., Associated Press, Accessed 10 November 2016. [Available online at: http://bigstory.ap.org/article/0d358e01ce4a442a9e7f10a254aaaed1/caribbean-braces-worsening-drought-dry-season-nears]

Coto, D. (2015b), Caribbean faces widespread drought, water shortages., Associated Press, Accessed 8 August 2016. [Available online at: http://bigstory.ap.org/urn:publicid:ap.org:eb72c16ff24c4459b6b08c4f24096e9c]

Daly, C., Gibson, W. P., Taylor, G. H., Johnson, G. L., & Pasteris, P. (2002). A knowledge-based approach to the statistical mapping of climate. *Climate Research*, *22*, 99–113. https://doi.org/10.3354/cr022099

Daly, C., Helmer, E. H., & Quiñones, M. (2003). Mapping the climate of Puerto Rico, Vieques and Culebra. *International Journal of Climatology*, *23*(11), 1359–1381. https://doi.org/10.1002/joc.937

Diak, G. R., Bland, W. L., & Mecikalski, J. R. (1996). A note on first estimates of surface insolation from GOES-8 visible satellite data. *Agricultural and Forest Meteorology*, *82*(1-4), 219–226. https://doi.org/10.1016/0168-1923(96)02331-3

Dunion, J. P. (2011). Rewriting the climatology of the Tropical North Atlantic and Caribbean Sea Atmosphere. *Journal of Climate*, *24*(3), 893–908. https://doi.org/10.1175/2010JCLI3496.1

Dunion, J. P., & Velden, C. S. (2004). The impact of the Saharan air layer on Atlantic tropical cyclone activity. *Bulletin of the American Meteorological Society*, *85*(3), 353–366. https://doi.org/10.1175/BAMS-85-3-353

Eck, T. F., Holben, B. N., Reid, J. S., Giles, D. M., Rivas, M. A., Singh, R. P., et al. (2012). Fog and cloud-induced aerosol modification observed by the Aerosol Robotic Network (AERONET). *Journal of Geophysical Research*, *117*, D07206. https://doi.org/10.1029/2011JD016839

Eltahir, E. A. B. (1998). A soil moisture-rainfall feedback mechanism: 1. Theory and observations. *Water Resources Research*, *34*(4), 765–776. https://doi.org/10.1029/97WR03499

Environmental Modeling Center/National Centers for Environmental Prediction/National Weather Service/NOAA/U.S. Department of Commerce (2015). NCEP North American Mesoscale (NAM) 12 km Analysis, http://rda.ucar.edu/datasets/ds609.0/, Research Data Archive at the National Center for Atmospheric Research, Computational and Information Systems Laboratory, Boulder, Colo. (Updated daily.) Accessed† 10 Feb 2019.

Feiser, E., (2015). Water, water everywhere? Caribbean adds to global drought., Bloomberg, Accessed 20 November 2016. [Available online at: http://www.bloomberg.com/news/articles/2015-07-10/water-water-everywhere-caribbean-adds-to-global-drought]

Food and Agriculture Organization of the United Nations (2016). *Drought characteristics and management in the Caribbean*, (p. 93). Rome, Italy: Caribbean Institute for Meteorology and Hydrology, St. James, Barbados and Land and Water Division, FAO. http://www.fao.org/3/a-i5695e.pdf

Gamble, D. W., & Curtis, S. (2008). Caribbean precipitation: Review, model, and prospect. *Progress in Physical Geography*, *32*(3), 265–276. https://doi.org/10.1177/0309133308096027

Gamble, D. W., Parnell, D. B., & Curtis, S. (2008). Spatial variability of the Caribbean mid-summer drought and relation to north Atlantic high circulation. *International Journal of Climatology*, *28*(3), 343–350. https://doi.org/10.1002/joc.1600

Gautier, C., Diak, G. R., & Masse, S. (1980). A simple physical model to estimate incident solar radiation at the surface from GOES satellite data. *Journal of Applied Meteorology*, *19*, 1007–1012.

Gelaro, R., McCarty, W., Suárez, M. J., Todling, R., Molod, A., Takacs, L., et al. (2017). The Modern-Era Retrospective Analysis for Research and Applications, version 2 (MERRA-2). *Journal of Climate*, *30*(14), 5419–5454. https://doi.org/10.1175/JCLI-D-16-0758.1

Giannini, A., Cane, M., & Yochanan, K. (2001). Interdecadal changes in the ENSO teleconnection to the Caribbean region and the North Atlantic Oscillation. *Journal of Climate*, *14*(13), 2867–2879. https://doi.org/10.1175/1520-0442(2001)014<2867:ICITET>2.0.CO;2

Giannini, A., Chiang, J., Cane, M., Kushnir, Y., & Seager, R. (2001). The ENSO teleconnection to the Tropical Atlantic Ocean: Contributions of the remote and local SSTs to rainfall variability in the Tropical Americas. *Journal of Climate*, *14*(24), 4530–4544. https://doi.org/10.1175/1520-0442(2001)014<4530:TETTTT>2.0.CO;2

Giannini, A., Kushnir, Y., & Cane, M. A. (2000). Interannual variability of Caribbean rainfall, ENSO, and the Atlantic Ocean. *Journal of Climate*, *13*(2), 297–311. https://doi.org/10.1175/1520-0442(2000)013<0297:IVOCRE>2.0.CO;2

Gómez-Gómez, F., Rodríguez-Martínez, J., & Santiago, M., (2014). Hydrogeology of Puerto Rico and the outlying islands of Vieques, Culebra, and Mona: U.S. Geological Survey Scientific Investigations Map 3296, 40 p. plus 2 pls. https://dx.doi.org/10.3133/sim3296

Gray, W. M. (1967). The mutual variation of wind, shear, and baroclinicity in the cumulus convective atmosphere of the hurricane. *Monthly Weather Review*, *95*(2), 55–73. https://doi.org/10.1175/1520-0493(1967)095<0055:TMVOWS>2.3.CO;2

Gray, W. M. (1968). Global view of the origin of tropical disturbances and storms. *Monthly Weather Review*, *96*(10), 669–700. https://doi.org/10.1175/1520-0493(1968)096<0669:GVOTOO>2.0.CO;2

Grist, J. P. (2002). Easterly Waves over Africa. Part I: The seasonal cycle and contrasts between wet and dry years. *Monthly Weather Review*, *130*(2), 197–211. https://doi.org/10.1175/1520-0493(2002)130<0197:EWOAPI>2.0.CO;2

Harmsen, E. W., Mecikalski, J., Cardona-Soto, M. J., Rojas Gonzalez, A., & Vasquez, R. (2009). Estimating daily evapotranspiration in Puerto Rico using satellite remote sensing. *WSEAS Transactions on Environment and Development*, *6*, 456–465.

Hart, J. A., & Korotky, W. D. (1991). *The SHARP Workstation - v1.50. A skew T/hodograph analysis and research program for the IBM and compatible PC. User's Manual*, (p. 62). Charleston, WV: NOAA/NWS Forecast Office.

Hastenrath, S. (1976). Variations in low-latitude circulation and extreme climatic events in the tropical Americas. *Journal of the Atmospheric Sciences*, *33*, 200–215.

Hastenrath, S. (1978). On modes of tropical circulation and climatic anomaly. *Journal of the Atmospheric Sciences*, *35*(12), 2222–2231. https://doi.org/10.1175/1520-0469(1978)035<2222:OMOTCA>2.0.CO;2

Hosannah, N., González, J. E., Rodriguez-Solis, R., Parsani, H., Moshary, F., Aponte, L., et al. (2017). The Convection, Aerosol, and Synoptic-Effects in the Tropics (CAST) experiment: Building an understanding of multi-scale impacts on Caribbean weather via field campaigns. *Bulletin of the American Meteorological Society*, *98*. https://doi.org/10.1175/BAMS-D-16-0192.1

Hosannah, N., Parsiani, H., & González, J. E. (2015). The role of aerosols in convective processes during the midsummer drought in the Caribbean. *Advances in Meteorology*, *2015*, 1–16. https://doi.org/10.1155/2015/261239

Hurrell, J. W. (1995). Decadal trends in the North Atlantic Oscillation and relationships to regional temperature and precipitation. *Science*, *269*(5224), 676–679. https://doi.org/10.1126/science.269.5224.676

Ismail, S., Ferrare, R. A., Browell, E. V., Chen, G., Anderson, B., Kooi, S. A., et al. (2010). LASE measurements of water vapor, aerosol, and cloud distributions in Saharan air layers and tropical disturbances. *Journal of the Atmospheric Sciences*, *67*(4), 1026–1047. https://doi.org/10.1175/2009JAS3136.1

Jaenicke, R., & Schütz, L. (1978). Comprehensive study of physical and chemical properties of the surface aerosols in the Cape Verde Islands region. *Journal of Geophysical Research*, *83*(C7), 3585–3599. https://doi.org/10.1029/JC083iC07p03585

Johns, R. H., & Doswell, C. A. III (1992). Severe local storms forecasting. *Weather and Forecasting*, *7*(4), 588–612. https://doi.org/10.1175/1520-0434(1992)007<0588:SLSF>2.0.CO;2

Jury, M. R. (2009). An intercomparison of observational, reanalysis, satellite, and coupled model data on mean rainfall in the Caribbean. *Journal of Hydrometeorology*, *10*(2), 413–430. https://doi.org/10.1175/2008JHM1054.1

Jury, M. R., & Chiao, S. (2013). Leeside boundary layer confluence and afternoon thunderstorms over Mayaguez, Puerto Rico. *Journal of Applied Meteorology and Climatology*, *52*(2), 439–454. https://doi.org/10.1175/JAMC-D-11-087.1

Jury, M. R., Chiao, S., & Harmsen, E. W. (2009). Mesoscale structure of trade wind convection over Puerto Rico: Composite observations and numerical simulation. *Boundary-Layer Meteorology*, *132*(2), 289–313. https://doi.org/10.1007/s10546-009-9393-3

Kalnay, E., Kanamitsu, M., Kistler, R., Collins, W., Deaven, D., Gandin, L., et al. (1996). The NCEP/NCAR 40-year reanalysis project. *Bulletin of the American Meteorological Society*, *77*(3), 437–471. https://doi.org/10.1175/1520-0477(1996)077<0437:TNYRP>2.0.CO;2

Keyantash, J., & Dracup, J. (2002). The quantification of drought: An evaluation of drought indices. *Bulletin of the American Meteorological Society*, *83*(8), 1167–1180. https://doi.org/10.1175/1520-0477-83.8.1167

Kingtse, M., Bell, G. D., & Thiaw, W. M. (2001). Impact of the sea surface temperature anomalies on the Atlantic tropical storm activity and West African rainfall. *Journal of the Atmospheric Sciences*, *58*, 3477–3496.

Knaff, J., Seseske, S., DeMaria, M., & Demuth, J. (2004). On the influences of vertical wind shear on symmetric tropical cyclone structure derived from AMSU. *Monthly Weather Review*, *132*(10), 2503–2510. https://doi.org/10.1175/1520-0493(2004)132<2503:OTIOVW>2.0.CO;2

Krause, P.F. & Flood, K.L. (1997). Weather and climate extremes, TEC-0099, US Army Corps of Engineers Topographic Engineering Center, 7701 Telegraph Road, Alexandra VA 22315-3864, 89 pp.

Landsea, C. W., Bell, G. D., Gray, W. M., & Goldenberg, S. B. (1998). The extremely active 1995 Atlantic hurricane season: Environmental conditions and verification of seasonal forecasts. *Monthly Weather Review*, *126*(5), 1174–1193. https://doi.org/10.1175/1520-0493(1998)126<1174:TEAAHS>2.0.CO;2

Litynska, Z., Parfiniewicz, J., & Pinkowski, H. (1976). The prediction of air mass thunderstorms and hails. *WMO*, *450*, 128–130.

Liu, C., & Moncrieff, M. W. (1996). A numerical study of the effects of ambient flow and shear on density currents. *Monthly Weather Review*, *124*, 2282–2303. https://doi.org/10.1175/1520-0493(1996)124<2282:ANSOTE>2.0.CO;2

Malmgren, B., Winter, A., & Chen, D. (1998). El Niño–Southern Oscillation and North Atlantic Oscillation control of the Puerto Rico climate. *Journal of Climate*, *11*(10), 2713–2717. https://doi.org/10.1175/1520-0442(1998)011<2713:ENOSOA>2.0.CO;2

McKee, T.B., Doesken, N. J., & Kliest, J. (1993). The relationship of drought frequency and duration to time scales. In Proceedings of the 8th Conference of Applied Climatology, 17-22 January, Anaheim, CA. American Meteorological Society, Boston, MA. 179-184.

Minder, J. R., Smith, R. B., & Nugent, A. D. (2013). The dynamics of ascent-forced orographic convection in the tropics: Results from Dominica. *Journal of the Atmospheric Sciences*, *70*(12), 4067–4088. https://doi.org/10.1175/JAS-D-13-016.1

Mote, T. L., Ramseyer, C. A., & Miller, P. W. (2017). The Saharan air layer as an early rainfall season suppressant in the eastern Caribbean: The 2015 Puerto Rico drought. *Journal of Geophysical Research: Atmospheres*, *122*, 10,966–10,982. https://doi.org/10.1002/2017JD026911

National Oceanic and Atmospheric Administration, (2014). Impacts of El Niño and La Niña on the hurricane season, causes climate change., Accessed 10 July 2017. [Available online at: https://www.climate.gov/news-features/blogs/enso/impacts-el-ni%C3%B1o-and-la-ni%C3%B1a-hurricane-season]

Nugent, A. D., Smith, R. B., & Minder, J. R. (2014). Wind speed control of tropical orographic convection. *Journal of the Atmospheric Sciences*, *71*(7), 2695–2712. https://doi.org/10.1175/JAS-D-13-0399.1

Otkin, J., Anderson, M. A., Mecikalski, J. R., & Diak, G. R. (2005). Validation of GOES-based insolation estimates using data from the United States climate reference network. *Journal of Hydrometeorology*, *6*, 475–640.

Pielke, R. A., Pitman, A., Niyogi, D., Mahmood, R., McAlpine, C., Hossain, F., & de Noblet, N. (2011). Land use/land cover changes and climate: Modeling analysis and observational evidence. *Wiley Interdisciplinary Reviews: Climate Change*, *2*(6), 828–850.

Population Reference Bureau, (2016). 2016 World population data sheet. Washington D.C., U.S.A. 22 pp. http://www.prb.org/pdf16/prb-wpds2016-web-2016.pdf

Prospero, J. M., & Carlson, T. N. (1972). Vertical and areal distribution of Saharan dust over the western equatorial North Atlantic Ocean. *Journal of Geophysical Research*, *77*(27), 5255–5265. https://doi.org/10.1029/JC077i027p05255

Prospero, J. M., & Lamb, P. J. (2003). African droughts and dust transport to the Caribbean: Climate change implications. *Science*, *302*(5647), 1024–1027. https://doi.org/10.1126/science.1089915

Qu, B., Gabric, A., Zhu, J., Lin, D., Qian, F., & Zhao, M. (2012). Correlation between sea surface temperature and wind speed in Greenland Sea and their relationships with NAO variability. *Water Science and Engineering*, *5*(3), 304–315.

Raman, S., Niyogi, D. S., Simpson, M., & Pelon, J. (2002). Dynamics of the elevated land plume over the Arabian Sea and the northern Indian Ocean during northeasterly monsoons and during the Indian Ocean experiment (INDOEX). *Geophysical Research Letters*, *29*(16), 1817. https://doi.org/10.1029/2001GL014193

Rauber, R. M., Stevens, B., Ochs, H. T. III, Knight, C., Albrecht, B. A., Blyth, A. M., et al. (2007). Rain in shallow cumulus over the ocean: The RICO campaign. *Bulletin of the American Meteorological Society*, *88*(12), 1912–1928. https://doi.org/10.1175/BAMS-88-12-1912

Reid, J. S., Douglas, L., Westphal, L., Livingston, J. M., Savoie, D. L., Maring, H. B., et al. (2002). Dust vertical distribution in the Caribbean during the Puerto Rico dust experiment. *Geophysical Research Letters*, *29*(7), 1151. https://doi.org/10.1029/2001GL014092

Rennick, M. A. (1976). The generation of African waves. *Journal of the Atmospheric Sciences*, *33*(10), 1955–1969. https://doi.org/10.1175/1520-0469(1976)033<1955:TGOAW>2.0.CO;2

Reynolds, R. W., Rayner, N. A., Smith, T. M., Stokes, D. C., & Wang, W. (2002). An improved in situ and satellite SST analysis for climate. *Journal of Climate*, *15*(13), 1609–1625. https://doi.org/10.1175/1520-0442(2002)

Rogers, J. C., & van Loon, H. (1979). The seesaw in winter temperatures between Greenland and northern Europe. Part II: Some oceanic and atmospheric effects in middle and high latitudes. *Monthly Weather Review*, *107*, 509–519.

Rosenfeld, D., Rudich, Y., & Lahav, R. (2001). Desert dust suppressing precipitation: A possible desertification feedback loop. *PNAS*, *98*(11), 5975–5980. https://doi.org/10.1073/pnas.101122798

Seo, D.-J. (1999). Real-time estimation of rainfall fields using radar rainfall and rain gauge data. *Journal of Hydrology*, *208*, 37–52.

Smith, R. B., Minder, J. R., Nugent, A. D., Storelvmo, T., Kirshbaum, D. J., Warren, R., et al. (2012). Orographic precipitation in the tropics: The Dominica Experiment. *Bulletin of the American Meteorological Society*, *93*(10), 1567–1579. https://doi.org/10.1175/BAMS-D-11-00194.1

Taylor, M. A., Enfield, D. B., & Chen, A. A. (2002). Influence of the tropical Atlantic versus the tropical Pacific on Caribbean rainfall. *Journal of Geophysical Research*, *107*(C9), 3127. https://doi.org/10.1029/2001JC001097

Thorncroft, C., & Hodges, K. (2001). African easterly wave variability and its relationship to Atlantic tropical cyclone activity. *Journal of Climate*, *14*(6), 1166–1179. https://doi.org/10.1175/1520-0442(2001)014<1166:AEWVAI>2.0.CO;2

United Nation Environment Programme (2008). Climate Change in the Caribbean and the challenge of adaptation. UNEP Regional Office for Latin America and the Caribbean, Panama City, Panama. 103 pp, http://www.pnuma.org/deat1/pdf/Climate_Change_in_the_Caribbean_Final_LOW20oct.pdf

van Loon, H., & Rogers, J. C. (1978). The seesaw in winter temperatures between Greenland and Northern Europe. Part I: General description. *Monthly Weather Review*, *106*, 296–310.

Walker, G. T., & Bliss, E. W. (1932). World weather V. *memoirs of the Royal Meteorological Society*, *4*(36), 53–84.

Wang, C. (2005). ENSO, Atlantic climate variability, and the Walker and Hadley circulations. In *Chapter 6 in The Hadley Circulation: Present, Past, and Future* (pp. 173–202). Netherlands: Kluwer Academic Publishers.

Wang, C., & Kirshbaum, D. J. (2015). Thermally forced convection over a mountainous tropical island. *Journal of the Atmospheric Sciences*, *72*, 2484–2506.

Waters, S. D. (2011), A classification index for precipitation events in Maricopa County, Arizona. 13 pp, http://alert.fcd.maricopa.gov/alert/MCS2I/MCS2I_whitepaper.pdf

Watson, C. D., Smith, R. B., & Nugent, A. D. (2015). Shallow, orographically triggered convection over Dominica: Observations from DOMEX. *Journal of the Atmospheric Sciences*, *72*, 3051–3072. https://doi.org/10.1175/JAS-D-14-0333.1

Weisman, M. L., and J. B. Klemp (1986), Characteristics of isolated convective storms. Mesoscale Meteorology and Forecasting. P. Ray, Ed., *Amer. Meteor. Soc.*, chap. 15, 504–520.

Williams, E., & Renno, N. (1993). An analysis of the conditional instability of the tropical atmosphere. *Monthly Weather Review*, *121*(1), 21–36. https://doi.org/10.1175/1520-0493(1993)121<0021:AAOTCI>2.0.CO;2

Wolter, K., & Timlin, M. S. (2011). El Niño/Southern Oscillation behaviour since 1871 as diagnosed in an extended multivariate ENSO index (MEI.ext). *International Journal of Climatology*, *31*(7), 1074–1087. https://doi.org/10.1002/joc.2336

Xie, P., & Arkin, P. A. (1997). Global precipitation: A 17-year monthly analysis based on gauge observations, satellite estimates, and numerical model outputs. *Bulletin of the American Meteorological Society*, *78*(11), 2539–2558. https://doi.org/10.1175/1520-0477(1997)078<2539:GPAYMA>2.0.CO;2

Yunhao, C., Xiaobing, L., & Peijun, S. (2001). Estimation of regional evapotranspiration over Northwest China by using remotely sensed data. *Journal of Geographical Sciences*, *11*, 140–148.